bioRxiv preprint doi: https://doi.org/10.1101/2021.07.07.451436; this version posted July 7, 2021. The copyright holder for this preprint (which was not certified by peer review) is the author/funder. All rights reserved. No reuse allowed without permission.

Distinct mitochondrial remodeling during early cardiomyocyte development in a human-based stem cell model

Sepideh Mostafavi (1)*, Novin Balafkan (1, 2) *†, Ina Katrine Nitschke Pettersen (3), Gonzalo S. Nido (1, 5), Richard Siller (4), Charalampos Tzoulis (1, 5), Gareth Sullivan (4, 6), Laurence A. Bindoff † (1, 5)

1) Department of Clinical Medicine, University of Bergen, Norway
2) Department of Mental Health Research, Haukeland University Hospital, Norway; Norwegian Centre for Mental Disorders Research (NORMENT) – Centre of Excellence, University of Oslo, Norway.
3) Institute for Biomedicine, University of Bergen, Norway
4) Stem Cell Epigenetics Laboratory, Institute of Basic Medical Sciences, University of Oslo, Norway
5) Neuro-SysMed, Center of Excellence for Clinical Research in Neurological Diseases, Department of Neurology, Haukeland University Hospital, Norway
6) Department of Molecular Medicine, Institute of Basic Medical Sciences, University of Oslo, Norway; Norwegian Center for Stem Cell Research, Oslo University Hospital and the University of Oslo, Norway; Institute of Immunology, Oslo University Hospital, Norway; Hybrid Technology Hub – Centre of Excellence, Institute of Basic Medical Sciences, University of Oslo, Norway; Department of Pediatric Research, Oslo University Hospital, Norway.

* These first authors contributed equally
† Corresponding authors with equal contribution

Corresponding authors:

Novin Balafkan Ph.D.,
Department of Mental Health Research
Haukeland University Hospital
Norway
Tel: +47 55958447
Fax: +47 55958447
e-mail: novin.balafkan@uib.no

Professor Laurence Bindoff
Department of Neurology
Haukeland University Hospital
5021, Bergen
Norway
Tel: +47 55975045
Fax: +47 55975064
e-mail: laurence.bindoff@nevro.uib.no

bioRxiv preprint doi: https://doi.org/10.1101/2021.07.07.451436; this version posted July 7, 2021. The copyright holder for this preprint (which was not certified by peer review) is the author/funder. All rights reserved. No reuse allowed without permission.

Summary statement

We found that differentiated cardiomyocytes have significantly lower level of mitochondria content compared to their original source, pluripotent stem cells, although the efficiency of ATP generation via mitochondria respiration increases.

Key words

Mitochondria, mtDNA, hPSC, hiPSC, OXPHOS, cardiomyocyte differentiation

Abstract

Post-mitotic tissues with high-energy demand rely on ATP generated by the mitochondrial respiratory chain through the process of oxidative phosphorylation (OXPHOS). There is common agreement that mitochondrial content and OXPHOS activity increase as cells exit from pluripotency state to meet the higher energy requirement of differentiated tissues such as heart. In this study, we examined the hypothesis that mitochondrial expansion during differentiation is necessary to compensate for higher energy demand in differentiated cells. We assessed mitochondrial and cellular metabolism during differentiation of human pluripotent stem cells to cardiac progenitors and further to functional cardiomyocytes. Contrary to expectations, we found that mitochondrial content decreased progressively during mesoderm differentiation. Nevertheless, we found that there was increased mitochondrial activity and higher levels of ATP-linked respiration, which we suggest more than compensate for the lower mitochondrial number. Our findings support a model whereby mitochondrial maturation during cardiomyocyte differentiation depends on increased efficiency of ATP generation through OXPHOS not increased mitochondrial biogenesis. Thus, the timing of the mitochondria expansion during cardiomyocyte differentiation will have to be revisited in light of these findings.

bioRxiv preprint doi: https://doi.org/10.1101/2021.07.07.451436; this version posted July 7, 2021. The copyright holder for this preprint (which was not certified by peer review) is the author/funder. All rights reserved. No reuse allowed without permission.

Introduction

Mitochondria are the major cellular source of ATP and in post-mitotic tissues with high-energy demand it is estimated that more than 90% of ATP is generated by the respiratory chain through oxidative phosphorylation (OXPHOS). In contrast, undifferentiated cells are highly dependent on aerobic glycolysis, with 70-90% of the consumed glucose accounted for as lactate (Varum et al., 2011; Zhang et al., 2012a). It has been suggested that high glycolytic flux supplies enough ATP and anabolic precursors to meet the requirements for the rapid proliferation of human pluripotent stem cells (hPSC) and cancer cells (Locasale and Cantley, 2011).

It is well established that as hPSCs exit pluripotency they undergo metabolic remodeling from a primarily glycolytic based metabolism to mitochondrial respiration (Folmes et al., 2012; Xu et al., 2013). Metabolic switching during differentiation is thought to be germ layer specific, as inhibition of glycolysis inhibits neuronal differentiation, but has no effect on mesoderm and endoderm differentiation (Cliff et al., 2017). Recently, a number of studies investigated the molecular pathways and alterations of mitochondria properties during ectoderm differentiation. Instead of simply comparing PSC with terminally differentiated cells, these studies focused on the three main stages of neuronal differentiation – pluripotency, neuronal progenitors cells (NPC), and functional neurons (Lees et al., 2018; Zheng et al., 2016) and identified a non-linear increase in mitochondrial content during ectoderm differentiation. Contrary to what was previously thought, they showed an initial drop in mitochondrial mass, mtDNA and superoxide production (Cho et al., 2006; John et al., 2005).

In order to gain greater insight into the role of mitochondria expansion in metabolic remodeling during mesoderm differentiation, we assessed mitochondrial abundance, ultrastructure, membrane potential, and respiratory complex activity during differentiation and maturation of cardiomyocytes derived from both human embryonic stem cells (hESC) and human induced pluripotent stem cells (hiPSC). Cardiomyocytes derived from hPSC share the characteristics and functional properties of primary human heart tissue and are able to recapitulate the *in vivo* developmental process (Friedman et al., 2018; Zhu et al., 2017; Zwi et al., 2009).

In contrast to previous reports, we detected a significant reduction in mitochondrial biomass and mtDNA levels during differentiation of hPSC towards cardiac progenitors and functional cardiomyocytes. Despite this marked mitochondrial reduction, however, differentiated cells showed a higher mitochondrial coupling efficiency and appeared more dependent on OXPHOS with a higher mitochondrial membrane potential per unit mitochondria than undifferentiated

bioRxiv preprint doi: https://doi.org/10.1101/2021.07.07.451436; this version posted July 7, 2021. The copyright holder for this preprint (which was not certified by peer review) is the author/funder. All rights reserved. No reuse allowed without permission.

hPSCs. Overall, our findings suggest a unique mitochondrial remodeling process for cardiomyocyte differentiation whereby mitochondrial biogenesis decreases during the transition from hPSC into differentiated cardiomyocytes, while the efficiency of ATP generation through OXPHOS increases in keeping with mitochondrial maturation.

RESULTS AND DISCUSSION

Cardiomyocyte differentiation and characterization. Two hESC lines (429 and 360) and three hiPSC lines (established from two independent Detroit 551 clones (clones 7 and 10), one CRL 2097 iPSC clone, CRL-8) were selected for cardiomyocyte differentiation in a 96-well plate format (Balafkan et al., 2020). For comparative purposes, we divided the differentiation process into phases based on the expression of cell-type-specific markers (Fig. 1A): pluripotent state (S1, day 0), mesendoderm cells (S2, day 1-2), cardiac mesoderm (S3, day 3), cardiac progenitor cells (S4 - day 5-7), functional cardiomyocyte (S5, day 12-15). The specific markers for the mesoderm cell lineage were assigned based on previous studies (Sturzu and Wu, 2011; Vliet et al., 2012). We have previously shown that cardiomyocytes differentiated using this protocol in a 96-well plate format are physiologically functional as determined by assessing different ion channels and beat interval (see Movie 1-2) (Balafkan et al., 2020). Initial transcriptomic profiling of cardiac progenitors derived from different hPSCs was performed with samples collected from four hiPSCs and two of the hESC lines (429 and 360) at pluripotent state (S1) and cardiac progenitor (S4) (Fig S1). In addition, to validate our gene expression analysis and further profile the transcriptomes of the critical stages of mesoderm differentiation including S5, an independent RNA-seq experiment was performed using a hESC line (H1), which solely used for transcriptomic analysis and not included in other set of experiments. RNA samples from three independent differentiations of H1 were collected at the following stages: pluripotent state (S1), mesendoderm state (S2), cardiac progenitor (S4) and functional cardiomyocyte (S5). Both data sets revealed downregulation of pluripotent stem cell markers, while up-regulated genes were enriched in pathways associated with cardiomyocyte differentiation including regulation of cardiac muscle, ventricular cardiac muscle tissue morphogenesis, sarcomere, and regulation of heart contraction (Fig. 1B and S1). The correct cardiomyocyte differentiation route was confirmed using qPCR (Fig. S1) and immunocytochemistry (Fig. 1C and 1D). This data indicates that our model is a reliable model to assess cardiomyocyte differentiation.

bioRxiv preprint doi: https://doi.org/10.1101/2021.07.07.451436; this version posted July 7, 2021. The copyright holder for this preprint (which was not certified by peer review) is the author/funder. All rights reserved. No reuse allowed without permission.

Previously, we have shown that differentiating cells in a 96-well plate format results in a population of both cardiomyocytes and non-cardiomyocytes, similar to what is expected in the composition of the mammalian heart (Sturzu and Wu, 2011). The TNNT2+ cells exhibit relevant electrophysiological properties and express specific cardiomyocyte markers, while the non-cardiac population consists of different mesodermal lineages such as smooth muscle and endothelial cells (Fig. S2) (Balafkan et al., 2020; Skelton et al., 2017). Thus, cells in S1 represent a pure population of PSCs (SSEA4+), S4 a relatively pure population of cardiac progenitors (ISL1+), while S5 comprises two different cell populations, TNNT2+ and TNNT2- cells, i.e. cardiomyocytes and non-cardiomyocyte cell populations (Fig. S2). The presence of both cardiomyocytes and non-cardiomyocytes is a particularly important aspect of our study since we have, for the first time, investigated the differences between two major cell subpopulations resulting from mesoderm differentiation.

Of note, since there were no significant differences in mitochondrial properties between hESCs and hiPSCs during cardiac differentiation, we pooled the results from the hiPSC and hESC lines for each stage. We demonstrated inter- and intra-individual variation for each set of experiments in supplementary data.

Mitochondrial content falls progressively during mesoderm differentiation. Thirteen polypeptides that are essential respiratory chain components are encoded by mtDNA. Unlike nuclear DNA, mtDNA is present in multiple copies and its copy number can impact the levels of mitochondrial RNA transcripts available for generating respiratory chain subunits (Anderson et al., 1981). We assessed the mtDNA copy number at different stages of cardiomyocyte differentiation using real-time PCR quantification relative to the nuclear gene *APP* (Tzoulis et al., 2013). This revealed a clear and progressive reduction of mtDNA copy number (of up to 85%) during differentiation of both hiPSC and hESC to cardiomyocyte lineage (Fig. 2A). Earlier studies have shown that the undifferentiated cells at the embryoblast stage have the lowest level of mtDNA level and mitochondria content (Taylor and Pikó, 1995), and spontaneous differentiation through formation of embryoid bodies resulted in an increase in mtDNA proliferation and mitochondria mass (Belmonte and Morad, 2008; Cho et al., 2006; John et al., 2005; Lukyanenko et al., 2009). For comparative purposes, we quantified mtDNA in post-mortem human heart using the same method and confirmed that the level of mtDNA in the mature tissue is at least 11-44 times higher than hPSCs and differentiated cells at S5 (Fig. 2B). More recent findings showed a higher level of mtDNA and mitochondria content in fully differentiated cells relative to undifferentiated cells derived from hPSC, which is aligned with

bioRxiv preprint doi: https://doi.org/10.1101/2021.07.07.451436; this version posted July 7, 2021. The copyright holder for this preprint (which was not certified by peer review) is the author/funder. All rights reserved. No reuse allowed without permission.

the transition from glycolytic state to a state with higher OXPHOS activity (Malinska et al., 2012; Wanet et al., 2014; Zheng et al., 2016). Others have found that mtDNA levels drop during ectoderm differentiation and reach their lowest levels in NPCs (Lees et al., 2018). Our findings showing low mtDNA level in cardiac progenitors (S4) is, therefore, similar to what has been reported in ectoderm differentiation (Lees et al., 2018), however, fact that the mtDNA levels did not rise in TNNT2+ cells relative to PSC was unexpected.

Assessed by bulk RNA-seq, we found that the majority of genes involved in mtDNA homeostasis decreased during mesoderm differentiation, including mtDNA maintenance exonuclease 1 (MGME1), single-stranded DNA binding protein (SSBP), mitochondrial transcription factor A (TFAM), and mtDNA helicase (TWNK) (Fig. 2C and Fig. S3). We validated RNA-seq findings by using real-time PCR to quantify the expression of *SSBP* and *POLG* that both have critical roles in mtDNA replication and were able to show a progressive decline of SSBP with no significant change in POLG expression level (Fig. S3). No evidence of qualitative damage such as mtDNA deletion was found at any stage of differentiation (Fig. S3F and G).

The link between the TFAM and mtDNA has been investigated in depth (Larsson et al., 1994; Larsson et al., 1998) and studies show that it binds mtDNA in molar quantities (Ekstrand et al., 2004; Kaufman et al., 2007; Kukat and Larsson, 2013). Using flow cytometry, we assessed TFAM both as a direct measure of a mitochondrial matrix protein and as an indirect measure of mtDNA level within each cell population co-stained with antibodies against stage-specific markers to validate our findings from real-time PCR. We found a 58% reduction of TFAM in cardiac progenitors (S4) relative to the pluripotent stage (S1) (Fig. 2D). Next, we examined changes in mitochondrial mass during cardiomyocyte differentiation at the single-cell level. We used flow cytometry and co-staining with antibodies against stage-specific markers and Translocase of Outer Mitochondrial Membrane 20 (TOMM20), a well-established marker of mitochondrial mass. The TOMM20 level showed a significant fall (43%) from S1 to S4 and reached its lowest level at S5 (60%) (Fig. 2E). As expected, the level of TOM20 was lower (~40%) in non-cardiomyocytes than cardiomyocytes (TNNT2+) indicating a lower level of mitochondria in non-cardiac cells. The results from each line for each stage of differentiation are shown in figure S4. The fall in mitochondrial mass starting from S3 was confirmed by a significant reduction of VDAC gene expression; VDAC encodes a vital outer membrane protein that is also routinely used as a mitochondrial mass marker (Fig. S3E). Given the link between the cell size and mitochondrial mass (Zheng et al., 2016), the finding of a lower

bioRxiv preprint doi: https://doi.org/10.1101/2021.07.07.451436; this version posted July 7, 2021. The copyright holder for this preprint (which was not certified by peer review) is the author/funder. All rights reserved. No reuse allowed without permission.

mitochondrial mass was surprising; differentiated cardiomyocytes are much larger cells than PSC (Fig. 1D-iv). A reduction of both mtDNA and mitochondria mass was previously found in the very early stage of ectoderm differentiation, but both started to increase from NPC onward (Birket et al., 2011; Lees et al., 2018; Zheng et al., 2016). A similar decline in mtDNA content has also been reported during hematopoietic differentiation (Almeida et al., 2017). Thus, our findings in cardiac progenitors suggest that the reduction of mtDNA levels and mitochondria content from pluripotent to multipotent stem cells may be a more general phenomenon than previously thought, and not limited to one specific cell lineage.

While levels of mitochondria and mtDNA appear to fall, metabolic changes occurring in terminally differentiated cells might still be tissue-specific. Our findings support the notion that the greater mitochondrial mass in PSC is not necessarily used for respiration (Almeida et al., 2017). Interestingly, when we measured changes in mtDNA level relative to mitochondrial content, by plotting the level of TFAM (an indirect marker of mtDNA) against TOM20 (a direct marker for mitochondrial content), we found that this ratio varied during the course of cardiomyocyte differentiation. The ratio of TFAM to TOM20 was significantly higher in differentiated cells in S5 relative to cardiac progenitors (S4) (Fig. 2F) suggesting that the lowest level of mtDNA per unit mitochondria mass occurred in cardiac progenitors and then rose in the more differentiated stage. These findings also highlight that mtDNA levels may not act as a proxy for mitochondrial level, particularly during differentiation, and it is important to use a complementary method to assess mitochondrial levels directly.

Despite lower mitochondrial content, differentiated cells generate more energy through TCA than glycolysis. Despite analyzing a heterogeneous population (TNNT2+ and TNNT2- cells), we were able to verify a significant increased expression of mtDNA genes in the S5 stage relative to other stages of differentiation (Fig. 3A) via bulk RNA-seq. These observations suggest that differentiated cells are relying more on mitochondrial respiration, regardless of the cell type they are committed to, and despite having much lower mitochondria mass.

We then assessed mitochondrial oxidative activity by measuring oxygen consumption rate (OCR) in differentiated cells at S5, which contain beating cardiomyocytes (see Movie 3-4), and in undifferentiated stem cells (S1) using Seahorse XF-96 extracellular flux analyzer (Fig 3C, 3D and Fig. S5). Interestingly, despite a major drop in mitochondrial mass, no major change in basal respiration, the amount of oxygen consumed by mitochondria under basal conditions, was detected: differentiated cells at S5 137 pmol/min, undifferentiated hPSCs at S1 148 pmol/min (Fig. 3E). Maximal OCR and spare capacity (also known as reserve capacity)

bioRxiv preprint doi: https://doi.org/10.1101/2021.07.07.451436; this version posted July 7, 2021. The copyright holder for this preprint (which was not certified by peer review) is the author/funder. All rights reserved. No reuse allowed without permission.

showed a slight increase in S5 compared to S1 cells (Fig. S5B and S5C). Coupling efficiency, the proportion of mitochondrial respiratory chain activity used to drive ATP synthesis (Divakaruni and Brand, 2011) was significantly higher (Fig 3F). The ratio of OCR to extracellular acidification rate (ECAR), an indicator of how much lactate is produced through glycolysis also rose in S5 cells relative to S1 suggesting a shift to mitochondrial respiration (Fig 3G). These findings corroborate previous studies showing the change in energy profile between PSC and terminally differentiated cells (Folmes et al., 2012). The finding of a negative value for spare capacity in hPSC lines (360 and CRL-8), raised the possibility that uncoupling by CCCP had collapsed the membrane potential in these lines (see blue bars in Fig. S5A-iv), and that, with a respiratory chain already working maximally, there was no further reserve capacity to be used with the extra stress (Varum et al., 2011; Zhang et al., 2012b).

We also investigated mitochondrial membrane potential (MMP) as a marker for mitochondrial activity. Membrane potential is generated by proton movement driven by the ETC and although MMP is an excellent marker for assessing mitochondrial function, it also reflects mitochondrial volume (Perry et al., 2011). Therefore, we employed a lipophilic cationic fluorescent probe tetramethylrhodamine methyl ester (TMRM) to evaluate MMP at the single-cell level by flow cytometry and normalized our data to mitochondria mass measured via TOM20 in the previous step. The absolute median fluorescent intensity (MFI) of TMRM was significantly lower at S5 relative to S1 (Fig. 3H and Fig. S5E), however, when we adjusted the MFI of TMRM for the mitochondrial mass, using the ratio of MFI-TMRM to MFI-TOM20, we found a more than two-fold increase in MMP at S5 compared with undifferentiated hPSCs at S1 (Fig. 3I and Fig. S5F). The significantly higher level of MMP per unit of mitochondrial mass in differentiated cells at S5 relative to undifferentiated hPSCs was further proof that the mitochondria in differentiated cells are more efficient in generating ATP.

Cristae remodeling during cardiomyocytes differentiation. We identified a significant increase in the expression of genes associated with mitochondrial biogenesis and respiration activities (e.g., PPARA, PPARG, PGC-1A and ESSRA, see figure 3B): since no increase in mitochondria mass was demonstrated (Fig. 2E), this suggested remodeling of mitochondrial membrane and cristae. We examined cells collected on S1, S4 and S5 by transmission electron microscopy (TEM) in order to assess the mitochondrial morphology and cristae structure. We observed that mitochondria went from having wide cristae with a dense matrix to having more compact cristae and clearer matrix (Fig. 3J). Previous findings have revealed that mitochondrial inner membrane morphology modulates OXPHOS function by modifying the kinetics of

bioRxiv preprint doi: https://doi.org/10.1101/2021.07.07.451436; this version posted July 7, 2021. The copyright holder for this preprint (which was not certified by peer review) is the author/funder. All rights reserved. No reuse allowed without permission.

chemical reactions and regulating the arrangement of protein complexes (Cogliati et al., 2016). It is also known that modulating cristae structure affects the mitochondrial respiratory efficiency independently of changes to mitochondrial protein synthesis (Cogliati et al., 2013). Our findings align with previous studies that reported the formation of cristae and mitochondrial permeability transition pore (mPTP) closure in differentiated cardiomyocytes, which are known characteristics of the developmental maturation of mitochondria (Dai et al., 2017; Hom et al., 2011; Teixeira et al., 2015).

Our work highlights the similarity in mitochondrial remodeling in the transitional path from pluripotent to multipotent state in ectodermal and mesodermal lineages, while at the same time suggesting differing cell-lineage-specific metabolic paths upon commitment to a specific cell lineage. This is in contrast to earlier studies that suggested a simultaneous expansion of mitochondrial content and increase in OXPHOS activity during differentiation. Interestingly, our findings also offer experimental validation for the previously proposed mathematical model that suggested cells modulate their mitochondrial membrane potential, rather than their mtDNA level, to quickly meet the changes in energy demands in mammalian cells (Aryaman et al., 2017; Miettinen and Björklund, 2016). Whether these findings are physiologically relevant or can be affected by the changes in signaling pathways at early stages of the differentiation protocol under the normoxic conditions remains an unanswered question.

ACKNOWLEDGMENTS

The authors wish to acknowledge the help and resources provided by the Flow Cytometry Core Facility, University of Bergen and the Molecular Imaging Center (MIC), Department of Biomedicine, University of Bergen. We would like to thank Tilo W. Eichler and Christian Dölle for helpful discussions. This work was supported by grants from The Research Council of Norway (NFR, project no. 229652), Bergen Stem Cell Consortium (BSCC), Haukeland University Hospital, University of Bergen and the Rakel og Otto-Kristian Bruun's Legat.

CONFLICT OF INTEREST

The authors declare that they have no conflict of interest.

bioRxiv preprint doi: https://doi.org/10.1101/2021.07.07.451436; this version posted July 7, 2021. The copyright holder for this preprint (which was not certified by peer review) is the author/funder. All rights reserved. No reuse allowed without permission.

AUTHOR CONTRIBUTIONS

Conceptualization: L.A.B, N.B.; **Methodology**: N.B., S.M., G.S.; **Software**: G.S.N.; **Validation and formal analysis**: N.B., S.M., G.S.N.; **Investigation**: S.M., N.B., I.K.N.P, R.S.; **Resources**: L.A.B, G.S., C.T.; **Data Curation**: G.S.N., N.B.; **Writing – original draft preparation:** N.B.; **Writing – review and editing**: L.A.B, N.B., S.M.; **Visualization**: S.M., N.B., G.S.N.; **Supervision**: L.A.B, N.B.; **Project administration and funding acquisition**: L.A.B.

MATERIALS AND METHODS

Cell lines. Three hESC lines (H1, 429 and 360) and four hiPSC lines (established from two independent Detroit 551 clones (clones 7 and 10), one CRL 2097 iPSC clone, CRL-8) were employed for this study. The details of reprogramming and characterization of the lines hiPSC published elsewhere (Balafkan et al., 2020; Liang et al., 2020).

Cardiomyocyte differentiation. Cardiomyocyte differentiation was performed in 96-well microplate as previously described (Balafkan et al., 2020). Briefly, hiPSCs were seeded at 2.4 x 10^4 cells/cm and propagated on Geltrex (#A1413302, Thermo Fisher Scientific) diluted (1:100) in Advanced DMEM/F-12 (#12634010, Thermo Fisher Scientific), under feeder free conditions in Essential 8 Medium (E8) (#A1517001, Thermo Fisher Scientific). Within 3 days, when cells reached the optimum confluency, 60 to 70%, cardiomyocyte differentiation was started by applying the GSK3 inhibitor CHIR99021 (#4423, Tocris Bioscience) in RPMI 1640 (#61870, Thermo Fisher Scientific) medium supplemented with B27-without insulin (RPMI-B27) (#A1895601, Thermo Fisher Scientific), in concentration-cell-dependent manner. After 24h, medium was changed to RPMI-B27 without CHIR99021. Differentiation process was continued by adding 5 µM inhibitor of WNT production-2, IWP2, (#3533, Tocris Bioscience) diluted in RPMI-B27, 72 hrs post differentiation induction for 48 hrs. Fresh RPMI-B27 medium was provided on day 5, and from day 7 cells were fed with fresh RPMI medium supplemented with B27 with insulin (#17504044, Thermo Fisher Scientific) without extra supplement) every two other days.

Gene expression analysis. MagMAX™-96 Total RNA Isolation Kit (#AM1830, Thermo Fisher Scientific) was used for RNA isolation from cultured cells. Cells were rinsed with DPBS (#14190250, ThermoFisher) and lysis buffer provided in the kit was added directly to the cells and lysates were either immediately used for RNA isolation using automated MagMAX

bioRxiv preprint doi: https://doi.org/10.1101/2021.07.07.451436; this version posted July 7, 2021. The copyright holder for this preprint (which was not certified by peer review) is the author/funder. All rights reserved. No reuse allowed without permission.

express 96 or stored at -80°C. EXPRESS One-Step Superscript qRT-PCR Kit (#11781-01K,Thermo Fisher Scientific) was used for cDNA synthesis and real-time PCR using TaqMan probes (Table S1) on an Applied Biosystems 7500-Fast real-time PCR System (Thermo Fisher Scientific). All real-time PCR reactions were performed in triplicate and the average of Ct values normalized to the geometric mean of ACTB and GAPDH as endogenous control genes, and the result (dCt) used for further analysis. Data was represented as the mean of 1/dCt with 95% CI of the mean and significance level of difference in expression of each gene at different time points was calculated using one-way ANOVA, whereas the difference between hiPSC and hESC lines at each time point was calculated using multiple t-test with Holm-Sidak correction for multiple comparison.

RNA sequencing. RNA sequencing was carried out on two different data sets, which analyzed independently and separately. Data set A, contains RNA sequences from both hESCs and hiPSC lines collected from S1(Undifferentiated cells-D0) and S4 (Cardiac-progenitors-D7) of cardiomyocyte differentiation. It composed of samples collected from three independent differentiation of two hESC lines (429 and 360), two independent differentiation of Detroit-7 and CRL-8, and one differentiation of Detroit-10. Data set B constitutes from RNA sequences collected from four stages S1-S5 (D0, D2, D5, and D15) of three independent differentiation runs of the H1 line (hESC). The total RNA samples were isolated using MagMAX™-96 Total RNA Isolation Kit.

RNA sequencing for the dataset (A) was carried out at the Finnish Microarray and Sequencing Centre's analysis service and Biocenter Finland. The quality of the total RNA samples and libraries was ensured with Advanced Analytical Fragment Analyzer. Sample concentration was measured with Qubit® Fluorometric Quantitation, Life Technologies. RNA quality as measured by RNA integrity number (RIN) was well above 7 for all samples (median RIN = 9,25) with the exception of a single sample, with RIN = 5.5. The samples were sequenced with Illumina HiSeq 3000 instrument. Single-read sequencing with 1 x 50 bp read length was used, followed by dual index 8 bp run. The base calling was performed using Illumina's standard bcl2fastq2 software, automatic adapter trimming was used. RNA sequencing for the second dataset (B) was carried out at the HudsonAlpha Genome Sequencing Center, USA. RNA quality as measured by RNA integrity number (RIN) was well above 7 for all samples (median RIN = 8,8).

RNA expression quantification and filtering. RNA sequencing analyses were performed independently for each of the datasets. Raw FASTQ files were assessed using fastQC version

bioRxiv preprint doi: https://doi.org/10.1101/2021.07.07.451436; this version posted July 7, 2021. The copyright holder for this preprint (which was not certified by peer review) is the author/funder. All rights reserved. No reuse allowed without permission.

0.11.8 (Andrews, 2010), and reads were mapped using Salmon version 1.3.0 (Patro et al., 2017) with the fragment-level GC bias correction option (-gcBias) against the GENCODE Release 32 (GRCh38.p13) reference transcriptome and the GRCh38 reference genome, including the whole genome as decoy sequences. Transcript quantification was collapsed to the gene-level using the R package tximport version 1.14.2 (Soneson et al., 2015) with default parameters and the GENCODE Release 32 (GRCh38.p13) annotation. Low-expressed genes (i.e. genes with less than 10 reads in more than 75% of the samples of the corresponding dataset) were filtered out, resulting in 19,273 genes in dataset A, of which 80% annotated as protein-coding, and 22,480 in dataset B (73% annotated as protein-coding).

Differential gene expression and functional enrichment analyses. Differential gene expression analyses were performed using the DESeq2 R package version 1.26 (Love et al., 2014) with default parameters. Samples from dataset A originated from different cell lines, and this was accounted for explicitly in the model by incorporating it as a covariate into the statistical model. Multiple hypothesis testing was performed with the default automatic filtering of DESeq2 followed by false discovery rate (FDR) calculation by the Benjamini-Hochberg procedure. Analyses were carried out independently for the two datasets. Genes were scored according to their significance by transforming the p-values to account for direction of change. In summary, for each gene, the up-regulated score (S_{up}) was calculated as $S_{up} = 1–p/2$ if LFC < 0, and $p/2$ if LFC≥0. The down-regulated score (S_{down}) as $S_{down} = 1–S_{up}$, where LFC corresponds to the log fold change and p to the nominal p-value of the gene. Genes were then tested for enrichment using alternatively $\log(S_{up})$ and $\log(S_{down})$ scores employing the gene score resampling method implemented in the ermineR package version 1.0.1, an R wrapper package for ermineJ (Gillis et al., 2010) with the complete Gene Ontology (GO) database annotation (Ashburner et al., 2000), the KEGG database (Kanehisa and Goto, 2000) and a curated version of mitocarta (Calvo et al., 2016; Gaare et al., 2018) to obtain lists of up- and down-regulated pathways for each cohort. The source code for the RNA sequencing analyses is available in the GitLab repository (https://git.app.uib.no/neuromics/cardiomyocytes-rna-seq) under the GPL public license v3.0.

Flow cytometry. Cells were washed in DPBS (#14190250, ThermoFisher) three times and dissociated into single cells suspension using TrypLE™ Express Enzyme (#12604013, Thermo Fisher Scientific) for 10-20 minutes at 37 °C and were collected in the micro centrifuge tube. After a quick wash with DPBS cells were stained with Zombie Red™ Fixable Viability Kit (#423110, BioLegend) according to manufacturer's instructions. Single cells were fixed with

bioRxiv preprint doi: https://doi.org/10.1101/2021.07.07.451436; this version posted July 7, 2021. The copyright holder for this preprint (which was not certified by peer review) is the author/funder. All rights reserved. No reuse allowed without permission.

4% (vol/vol) paraformaldehyde for 10 min at room temperature (RT) and permeabilized for 10 min at -20°C with 90% ice-cold methanol diluted in PBS. Cells were blocked in blocking buffer consisting of 0.3 M glycine, 5% goat serum and 1% BSA in PBS for 20min at RT. The optimal concentration of conjugated antibodies for flow cytometry reported by the supplier for each batch was used. Antibodies are listed in Supplementary Table (Table S1). All the primary and secondary antibodies as well as conjugated antibodies diluted in blocking buffer and stained for 30 min at RT. Cells were washed after staining and collected in 300 µl of 1% FBS in PBS. Samples were analysed quickly after staining. At least 30.000 events were collected for the target marker using a Sony cell sorter SH800 (Sony Biotechnology Inc.) and collected data analysed and presented by FlowJo V.10.5.0 (FlowJo LLC, OR, USA, www.FlowJo.com) 8-Peaks Rainbow Calibration Particles (Biolegend #422903) was used for routine alignment and performance verification of the flow cytometry. The flow cytometer was calibrated prior to quantitative fluorescence intensity measurements using Quantum™ Alexa Fluor® 488 MESF (molecules of equivalent soluble fluorophore) (Bangs Laboratories, Inc. #488). In order to test the integrity of the results over time, collected median fluorescence intensity (MFI) was normalized to MESF as an external control and the resulting values reported as relative MFI to MESF unit. All gates were adjusted according to fluorescence minus one control (FMO). To analyse the flow cytometry data the median values of MESF were used to compare the samples and 95% CI of the median used to show the confidence in median value.

Immunocytochemistry and fluorescence microscopy. Cells were seeded either on Geltrex coated cover slips or in Millicell® EZ SLIDES (#PEZGS0816, Merck Millipore). Cells were fixed with 4% (vol/vol) paraformaldehyde for 10 min at RT and permeabilized with 0.3% Tween 20 (#822184, Merck Millipore). All the primary and secondary antibodies were diluted in blocking buffer consisting of 0.3 M glycine, 5% goat serum and 1% BSA in PBS. A final concentration of 10 µg/ml was used for all primary antibodies and they were incubated overnight at 4°C. Alexa Fluor 488 or 594-conjugated (Thermo Fisher Scientific) secondary antibodies were diluted in blocking buffer 1:1000 and incubated for 30 min to 1h at room temperature. Nuclei were stained with Gold Antifade Reagent with DAPI (#P36935, Thermo Fisher Scientific). Confocal microscopy images were taken on eighter a Zeiss LSM 510 META or a Leica TCS SP5 at the Molecular Imaging Center (MIC), University of Bergen, and data analysis and image editing were done with Fiji (Schindelin et al., 2012). Antibodies are listed in Supplementary table (Table S1).

bioRxiv preprint doi: https://doi.org/10.1101/2021.07.07.451436; this version posted July 7, 2021. The copyright holder for this preprint (which was not certified by peer review) is the author/funder. All rights reserved. No reuse allowed without permission.

Transmission Electron Microscopy. Cells were washed in DPBS and dissociated into single cells suspension using TrypLE™ Express Enzyme for 10-20 minutes at 37°C and were collected in the micro centrifuge tube and centrifuged at 300 g for 10 min at RT. Cells were fixed in 2,5% glutaraldehyde (diluted in a 0,1M sodium cacodylate buffer) for 24 hrs at 4°C and delivered to MIC facility at the University of Bergen. Post-fixation was performed for 1h (on ice) in 1% osmium tetroxide (EMS # 19134) diluted in 0,1 M sodium cacodylate buffer, followed by 2 washing steps. The samples were then dehydrated using a graded ethanol series (30%, 50%, 70%, 96% and 100%) before transferred to a 1:1 solution of 100% ethanol:propylene oxide (15 min). Samples were then transferred to 100% propylene oxide (15min) before gradually introducing agar 100 resin (AgarScientific R1031) drop by drop over the next hours. Samples were then transferred to a small drop of 100% resin and excess propylenoxid was allowed to evaporate (1h). Samples were then transferred to 100% resin and placed in molds and left in room temperature overnight. The molds were then placed at 60°C for 48h to polymerize. Ultrasections of approximately 60nm were placed on 100 mesh formvar coated(EMD # 15820) kopper grids (EMS #G100H-Cu) and stained with 2% uranyl acetate (EMS # 22400) and lead citrate (VWR #1.07398). Grids were imaged using a Jeol JEM-1230 transmission electron microscope at 80kV.

MtDNA analysis. MtDNA quantification and deletion assessment was performed in DNA isolated from cultured cells using MagMAX™-96 DNA Multi-Sample Kit (#4413021, Thermo Fisher Scientific) and real-time PCR, as well as long range PCR, as previously described (Tzoulis et al., 2013). A commonly deleted region (MT-ND4) in the major arc of mitochondrial DNA and a rarely deleted region (MT-ND1) were utilized to quantify deletion and MT-ND1 was compared with amplification of a single-copy nuclear gene (APP) to assess the number of mtDNA copies. A triplex reaction of ND1, ND4 and APP was performed simultaneously within the same well using a 7500 fast sequence detection system (Thermo Fisher Scientific). Efficiency of the triplex reaction was measured prior sample analysis. Assessment of statistical significance was performed using one-way ANOVA with Dunnett's post-hoc multiple comparisons.

Measurement of OCR and ECAR using Seahorse XF-96 analyser. Respiration and acidification rates were measured on monolayer culture of undifferentiated hPSCs and cells at S5 using a Seahorse XFe96 extracellular flux analyser (Agilent, Santa Clara, CA, US). Geltrex coated XFe96 assay plates were utilized for seeding of $3x10^3$ undifferentiated hPSCs and $2x10^5$ hPSC-derived cardiac cells in each well. Cells were cultured in cell specific normal growth

bioRxiv preprint doi: https://doi.org/10.1101/2021.07.07.451436; this version posted July 7, 2021. The copyright holder for this preprint (which was not certified by peer review) is the author/funder. All rights reserved. No reuse allowed without permission.

medium supplemented with 10 µM of Y-27632 for 24 hours at 37 °C and 5% CO_2). The next day, the supplemented growth medium was replaced with normal growth medium without supplement and kept till they reached almost 90% confluency prior to analysis. In order to find the optimal concentration of Carbonyl cyanide m-chlorophenyl hydrazone (CCCP) and oligomycin for each cell type, they were titrated prior to the cell analysis. The assay was performed in assay medium (pH 7.4, unbuffered) which was supplemented with 2 mM L-glutamine, 2 mM sodium pyruvate and 10 mM glucose. Cells were washed twice and pre-incubated in the assay medium and kept in a CO2-free incubator (XF Prep Station, Seahorse Biosciences) at 37°C for 1 hour before measurement, in order to remove CO_2 from the medium. For mitochondrial respiration analysis, the final concentrations of 3 µM oligomycin, 0.5-1 µM CCCP, 1 µM rotenone and 1 µM antimycin A were diluted in assay medium. In order to correct the final results for differences in cell size and number between the undifferentiated hPSCs and differentiated cells at S5 we measured the total protein concentration for each well using absorbance at 280 nm. All the results were reported as pmol O_2 per min after normalized to their total protein concentration. Each parameter was calculated accordingly; basal OCR= (OCR in non-treated cell – OCR after adding Antimycin A), Coupling Efficiency = (ATP Production Rate / Basal Respiration Rate × 100), spare respiration capacity = (maximal respiration / basal respiration). The XF reader software (Wave Desktop 2.4) was used to analyses the data.

Measurement of mitochondrial membrane potential. We used a previously described protocol (Rowe and Boletta, 2013) to analyse the mitochondrial membrane potential (ψm) independent of cell volume using TMRM. We quantified the fluorescent intensity of TMRM (FI) before and after applying Carbonyl cyanide 4-(trifluoromethoxy)phenylhydrazone (FCCP) as an uncoupler for OXPHOS which eliminates the mitochondrial membrane potential. The distribution of TMRM rely on the Nernstian equilibrium (Dykens and Stout, 2001). Accumulation of TMRM in the cytosol is very small compare with mitochondria due to the low negative charge of cytosol relative to mitochondrial matrix. Thus, fluorescence readout mirror the mitochondrial matrix:cell volume ratio. FCCP treatment of the cell releases the TMRM from mitochondrial matrix into cytosol and causes a re-equilibrium of TMRM in the cytosol. Therefore, fluorescence readout after FCCP treatment represents cell volume. The difference between geometric means for TMRM and TMRM-FCCP treated cells provided us the membrane potential level normalized to the cell size. We analysed mitochondrial membrane potential by flow cytometry starting with $1x10^6$ cells per sample. Each sample

bioRxiv preprint doi: https://doi.org/10.1101/2021.07.07.451436; this version posted July 7, 2021. The copyright holder for this preprint (which was not certified by peer review) is the author/funder. All rights reserved. No reuse allowed without permission.

divided in two; one sample was treated with 25nM TMRM and another with a mixture of 25 nM TMRM and 100 µM FCCP. Samples were incubated for 20 min at 37 °C and 5% CO_2 washed three times with HBSS and analysed within 1 hour.

Statistical tests. Data were expressed as mean or median with 95%CI of the mean or median depending on population distribution. To assess statistical significance, we used parametric tests; Student's t test and ANOVA, and P values corrected with a multiple test correction by with Holm-Sidak and Dunnetts accordingly. The significance of median difference was assessed using non-parametric test; Kruskal-Wallis and Mann Whitney test followed by Dunn's multiple correction. Data were analysed using GraphPad-Prism (Prism 7.0, GraphPad Software, La Jolla California USA).

BIBLIOGRAPHY

Almeida, M. J. de, Luchsinger, L. L., Corrigan, D. J., Williams, L. J. and Snoeck, H.-W. (2017). Dye-Independent Methods Reveal Elevated Mitochondrial Mass in Hematopoietic Stem Cells. *Cell Stem Cell* **21**, 725-729.e4.

Anderson, S., Bankier, A. T., Barrell, B. G., Bruijn, M. H. L. de, Coulson, A. R., Drouin, J., Eperon, I. C., Nierlich, D. P., Roe, B. A., Sanger, F., et al. (1981). Sequence and organization of the human mitochondrial genome. *Nature* **290**, 457–465.

Andrews, S. (2010). FastQC: a quality control tool for high throughput sequence data.

Aryaman, J., Hoitzing, H., Burgstaller, J. P., Johnston, I. G. and Jones, N. S. (2017). Mitochondrial heterogeneity, metabolic scaling and cell death. *Bioessays* **39**, 1700001.

Ashburner, M., Ball, C. A., Blake, J. A., Botstein, D., Butler, H., Cherry, J. M., Davis, A. P., Dolinski, K., Dwight, S. S., Eppig, J. T., et al. (2000). Gene ontology: tool for the unification of biology. The Gene Ontology Consortium. *Nat Genet* **25**, 25–9.

Balafkan, N., Mostafavi, S., Schubert, M., Siller, R., Liang, K. X., Sullivan, G. and Bindoff, L. A. (2020). A method for differentiating human induced pluripotent stem cells toward functional cardiomyocytes in 96-well microplates. *Sci Rep-uk* **10**, 18498.

Belmonte, S. and Morad, M. (2008). Shear fluid-induced Ca2+ release and the role of mitochondria in rat cardiac myocytes. *Ann Ny Acad Sci* **1123**, 58–63.

Birket, M. J., Orr, A. L., Gerencser, A. A., Madden, D. T., Vitelli, C., Swistowski, A., Brand, M. D. and Zeng, X. (2011). A reduction in ATP demand and mitochondrial activity with neural differentiation of human embryonic stem cells. *J Cell Sci* **124**, 348–58.

Calvo, S. E., Clauser, K. R. and Mootha, V. K. (2016). MitoCarta2.0: an updated inventory of mammalian mitochondrial proteins. *Nucleic Acids Res* **44**, D1251-7.

bioRxiv preprint doi: https://doi.org/10.1101/2021.07.07.451436; this version posted July 7, 2021. The copyright holder for this preprint (which was not certified by peer review) is the author/funder. All rights reserved. No reuse allowed without permission.

Cho, Y. M., Kwon, S., Pak, Y. K., Seol, H. W., Choi, Y. M., Park, D. J., Park, K. S. and Lee, H. K. (2006). Dynamic changes in mitochondrial biogenesis and antioxidant enzymes during the spontaneous differentiation of human embryonic stem cells. *Biochem Bioph Res Co* **348**, 1472–8.

Cliff, T. S., Wu, T., Boward, B. R., Yin, A., Yin, H., Glushka, J. N., Prestegaard, J. H. and Dalton, S. (2017). MYC Controls Human Pluripotent Stem Cell Fate Decisions through Regulation of Metabolic Flux. *Cell Stem Cell* **21**, 502-516.e9.

Cogliati, S., Frezza, C., Soriano, M. E., Varanita, T., Quintana-Cabrera, R., Corrado, M., Cipolat, S., Costa, V., Casarin, A., Gomes, L. C., et al. (2013). Mitochondrial cristae shape determines respiratory chain supercomplexes assembly and respiratory efficiency. *Cell* **155**, 160–71.

Cogliati, S., Enriquez, J. A. and Scorrano, L. (2016). Mitochondrial Cristae: Where Beauty Meets Functionality. *Trends Biochem Sci* **41**, 261–273.

Dai, D. F., Danoviz, M. E., Wiczer, B., Laflamme, M. A. and Tian, R. (2017). Mitochondrial Maturation in Human Pluripotent Stem Cell Derived Cardiomyocytes. *Stem Cells Int* **2017**, 5153625.

Divakaruni, A. S. and Brand, M. D. (2011). The regulation and physiology of mitochondrial proton leak. *Physiology* **26**, 192–205.

Dykens, J. A. and Stout, A. K. (2001). Assessment of mitochondrial membrane potential in situ using single potentiometric dyes and a novel fluorescence resonance energy transfer technique. **65**, 285–309.

Ekstrand, M. I., Falkenberg, M., Rantanen, A., Park, C. B., Gaspari, M., Hultenby, K., Rustin, P., Gustafsson, C. M. and Larsson, N. G. (2004). Mitochondrial transcription factor A regulates mtDNA copy number in mammals. *Hum Mol Genet* **13**, 935–44.

Focus on neuroscience methods (2020). *Nat Neurosci* **23**, 1455–1455.

Folmes, C. D., Dzeja, P. P., Nelson, T. J. and Terzic, A. (2012). Metabolic plasticity in stem cell homeostasis and differentiation. *Cell Stem Cell* **11**, 596–606.

Friedman, C. E., Nguyen, Q., Lukowski, S. W., Helfer, A., Chiu, H. S., Miklas, J., Levy, S., Suo, S., Han, J. J., Osteil, P., et al. (2018). Single-Cell Transcriptomic Analysis of Cardiac Differentiation from Human PSCs Reveals HOPX-Dependent Cardiomyocyte Maturation. *Cell Stem Cell* **23**, 586-598 e8.

Gaare, J. J., Nido, G. S., Sztromwasser, P., Knappskog, P. M., Dahl, O., Lund-Johansen, M., Maple-Grodem, J., Alves, G., Tysnes, O. B., Johansson, S., et al. (2018). Rare genetic variation in mitochondrial pathways influences the risk for Parkinson's disease. *Movement Disord* **33**, 1591–1600.

Gillis, J., Mistry, M. and Pavlidis, P. (2010). Gene function analysis in complex data sets using ErmineJ. *Nat Protoc* **5**, 1148–59.

Hom, J. R., Quintanilla, R. A., Hoffman, D. L., Bentley, K. L. de M., Molkentin, J. D., Sheu, S. S. and A., Jr. P., G. (2011). The permeability transition pore controls cardiac mitochondrial maturation and myocyte differentiation. *Dev Cell* **21**, 469–78.

bioRxiv preprint doi: https://doi.org/10.1101/2021.07.07.451436; this version posted July 7, 2021. The copyright holder for this preprint (which was not certified by peer review) is the author/funder. All rights reserved. No reuse allowed without permission.

John, J. C. S., Ramalho-Santos, J., Gray, H. L., Petrosko, P., Rawe, V. Y., Navara, C. S., Simerly, C. R. and Schatten, G. P. (2005). The expression of mitochondrial DNA transcription factors during early cardiomyocyte in vitro differentiation from human embryonic stem cells. *Cloning Stem Cells* **7**, 141–53.

Kanehisa, M. and Goto, S. (2000). KEGG: kyoto encyclopedia of genes and genomes. *Nucleic Acids Res* **28**, 27–30.

Kaufman, B. A., Durisic, N., Mativetsky, J. M., Costantino, S., Hancock, M. A., Grutter, P. and Shoubridge, E. A. (2007). The mitochondrial transcription factor TFAM coordinates the assembly of multiple DNA molecules into nucleoid-like structures. *Mol Biol Cell* **18**, 3225–3236.

Kukat, C. and Larsson, N. G. (2013). mtDNA makes a U-turn for the mitochondrial nucleoid. *Trends Cell Biol* **23**, 457–63.

Larsson, N. G., Oldfors, A., Holme, E. and Clayton, D. A. (1994). Low levels of mitochondrial transcription factor A in mitochondrial DNA depletion. *Biochem Bioph Res Co* **200**, 1374–81.

Larsson, N. G., Wang, J. M., Wilhelmsson, H., Oldfors, A., Rustin, P., Lewandoski, M., Barsh, G. S. and Clayton, D. A. (1998). Mitochondrial transcription factor A is necessary for mtDNA maintenance and embryogenesis in mice. *Nature Genetics* **18**, 231–236.

Lees, J. G., Gardner, D. K. and Harvey, A. J. (2018). Mitochondrial and glycolytic remodeling during nascent neural differentiation of human pluripotent stem cells. *Development* **145**, dev168997.

Liang, K. X., Kristiansen, C. K., Mostafavi, S., Vatne, G. H., Zantingh, G. A., Kianian, A., Tzoulis, C., Hoyland, L. E., Ziegler, M., Perez, R. M., et al. (2020). Disease-specific phenotypes in iPSC-derived neural stem cells with POLG mutations. *Embo Mol Med* **12**, e12146.

Locasale, J. W. and Cantley, L. C. (2011). Metabolic Flux and the Regulation of Mammalian Cell Growth. *Cell Metab* **14**, 443–451.

Love, M. I., Huber, W. and Anders, S. (2014). Moderated estimation of fold change and dispersion for RNA-seq data with DESeq2. *Genome Biol* **15**, 550.

Lukyanenko, V., Chikando, A. and Lederer, W. J. (2009). Mitochondria in cardiomyocyte Ca2+ signaling. *Int J Biochem Cell Biology* **41**, 1957–71.

Malinska, D., Kudin, A. P., Bejtka, M. and Kunz, W. S. (2012). Changes in mitochondrial reactive oxygen species synthesis during differentiation of skeletal muscle cells. *Mitochondrion* **12**, 144–8.

Miettinen, T. P. and Björklund, M. (2016). Cellular Allometry of Mitochondrial Functionality Establishes the Optimal Cell Size. *Dev Cell* **39**, 370–382.

Patro, R., Duggal, G., Love, M. I., Irizarry, R. A. and Kingsford, C. (2017). Salmon provides fast and bias-aware quantification of transcript expression. *Nat Methods* **14**, 417–419.

Perry, S. W., Norman, J. P., Barbieri, J., Brown, E. B. and Gelbard, H. A. (2011). Mitochondrial membrane potential probes and the proton gradient: a practical usage guide. *Biotechniques* **50**, 98–115.

bioRxiv preprint doi: https://doi.org/10.1101/2021.07.07.451436; this version posted July 7, 2021. The copyright holder for this preprint (which was not certified by peer review) is the author/funder. All rights reserved. No reuse allowed without permission.

Rowe, I. and Boletta, A. (2013). Mitochondrial Transmembrane Potential (ψm) Assay Using TMRM. *Bio-protocol* 3,.

Scarpulla, R. C., Vega, R. B. and Kelly, D. P. (2012). Transcriptional integration of mitochondrial biogenesis. *Trends Endocrinol Metabolism* **23**, 459–66.

Skelton, R. J. P., Kamp, T. J., Elliott, D. A. and Ardehali, R. (2017). Biomarkers of Human Pluripotent Stem Cell-Derived Cardiac Lineages. *Trends Mol Med* **23**, 651–668.

Soneson, C., Love, M. I. and Robinson, M. D. (2015). Differential analyses for RNA-seq: transcript-level estimates improve gene-level inferences. *F1000research* **4**, 1521.

Sturzu, A. C. and Wu, S. M. (2011). Developmental and regenerative biology of multipotent cardiovascular progenitor cells. *Circ Res* **108**, 353–64.

Taylor, K. D. and Pikó, L. (1995). Mitochondrial biogenesis in early mouse embryos: Expression of the mRNAs for subunits IV, Vb, and VIIc of cytochrome c oxidase and subunit 9 (P1) of H+-ATP synthase. *Mol Reprod Dev* **40**, 29–35.

Teixeira, F. K., Sanchez, C. G., Hurd, T. R., Seifert, J. R., Czech, B., Preall, J. B., Hannon, G. J. and Lehmann, R. (2015). ATP synthase promotes germ cell differentiation independent of oxidative phosphorylation. *Nat Cell Biol* **17**, 689–96.

Tzoulis, C., Tran, G. T., Schwarzlmuller, T., Specht, K., Haugarvoll, K., Balafkan, N., Lilleng, P. K., Miletic, H., Biermann, M. and Bindoff, L. A. (2013). Severe nigrostriatal degeneration without clinical parkinsonism in patients with polymerase gamma mutations. *Brain* **136**, 2393–2404.

Varum, S., Rodrigues, A. S., Moura, M. B., Momcilovic, O., Easley, C. A., Ramalho-Santos, J., Houten, B. V. and Schatten, G. (2011). Energy Metabolism in Human Pluripotent Stem Cells and Their Differentiated Counterparts. *Plos One* **6**, e20914.

Vliet, P. V., Wu, S. M., Zaffran, S. and Puceat, M. (2012). Early cardiac development: a view from stem cells to embryos. *Cardiovasc Res* **96**, 352–62.

Wanet, A., Remacle, N., Najar, M., Sokal, E., Arnould, T., Najimi, M. and Renard, P. (2014). Mitochondrial remodeling in hepatic differentiation and dedifferentiation. *Int J Biochem Cell Biology* **54**, 174–85.

Xu, X., Duan, S., Yi, F., Ocampo, A., Liu, G.-H. and Izpisua Belmonte, J. C. (2013). Mitochondrial Regulation in Pluripotent Stem Cells. *Cell Metab* **18**, 325–332.

Zhang, J., Nuebel, E., Daley, G. Q., Koehler, C. M. and Teitell, M. A. (2012a). Metabolic Regulation in Pluripotent Stem Cells during Reprogramming and Self-Renewal. *Cell Stem Cell* **11**, 589–595.

Zhang, J., Nuebel, E., Wisidagama, D. R., Setoguchi, K., Hong, J. S., Horn, C. M. V., Imam, S. S., Vergnes, L., Malone, C. S., Koehler, C. M., et al. (2012b). Measuring energy metabolism in cultured cells, including human pluripotent stem cells and differentiated cells. *Nat Protoc* **7**, 1068–85.

bioRxiv preprint doi: https://doi.org/10.1101/2021.07.07.451436; this version posted July 7, 2021. The copyright holder for this preprint (which was not certified by peer review) is the author/funder. All rights reserved. No reuse allowed without permission.

Zheng, X., Boyer, L., Jin, M., Mertens, J., Kim, Y., Ma, L., Ma, L., Hamm, M., Gage, F. H. and Hunter, T. (2016). Metabolic reprogramming during neuronal differentiation from aerobic glycolysis to neuronal oxidative phosphorylation. *Elife* **5**, e13374.

Zhu, H., Scharnhorst, K. S., Stieg, A. Z., Gimzewski, J. K., Minami, I., Nakatsuji, N., Nakano, H. and Nakano, A. (2017). Two dimensional electrophysiological characterization of human pluripotent stem cell-derived cardiomyocyte system. *Sci Rep-uk* **7**, 43210.

Zwi, L., Caspi, O., Arbel, G., Huber, I., Gepstein, A., Park, I. H. and Gepstein, L. (2009). Cardiomyocyte differentiation of human induced pluripotent stem cells. *Circulation* **120**, 1513–23.

bioRxiv preprint doi: https://doi.org/10.1101/2021.07.07.451436; this version posted July 7, 2021. The copyright holder for this preprint (which was not certified by peer review) is the author/funder. All rights reserved. No reuse allowed without permission.

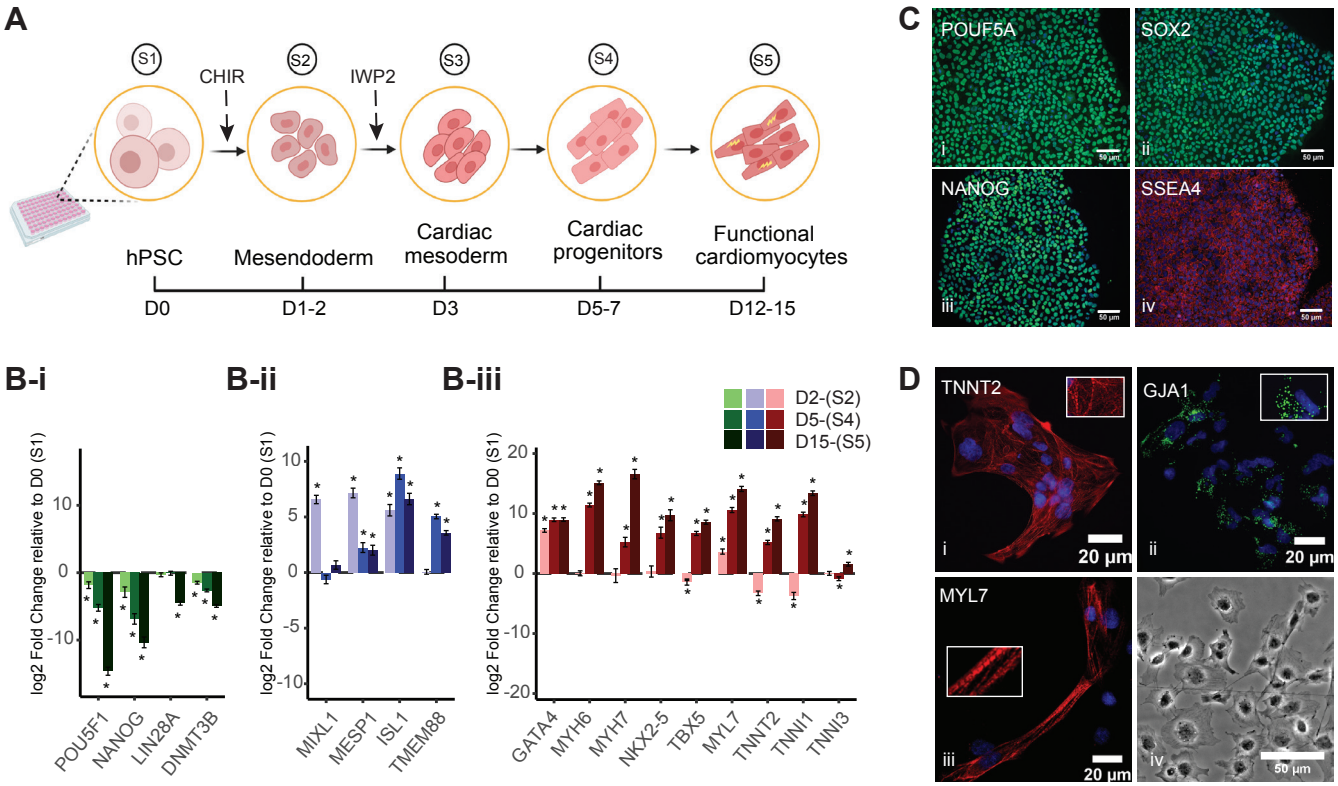

Figure 1) Cardiomyocyte differentiation and characterization. A) Schematic diagram of the cardiomyocyte differentiation protocol. Cells were treated with 6 μM (hiPSCs) or 8 μM (hESCs) CHIR99021 (CHIR) on day 1 for 24 h followed by treatment with IWP2, a Wnt signaling inhibitor, for 48 h on day 3. We divided cardiomyocyte differentiation into five different stages (S1-S5) for comparative purposes. B) Relative expression of known markers for stem cells (B-i), cardiac progenitor (B-ii) and cardiomyocytes (B-iii) haven been assessed using RNAseq data from H1 (n=3). C and D) Both hPSCs and hPSC-derived cardiomyocytes examined for expression of specific markers using a battery of antibodies. Pictures show co-immunostaining of the cell specific markers (labelled on the image) and nucleus (blue), E-iv represents a bright field image of cardiac cells at S5 (transferred from a 96-well plate to cover glass at S4). Scale bars demonstrates 50μm, otherwise are mentioned on the picture.

bioRxiv preprint doi: https://doi.org/10.1101/2021.07.07.451436; this version posted July 7, 2021. The copyright holder for this preprint (which was not certified by peer review) is the author/funder. All rights reserved. No reuse allowed without permission.

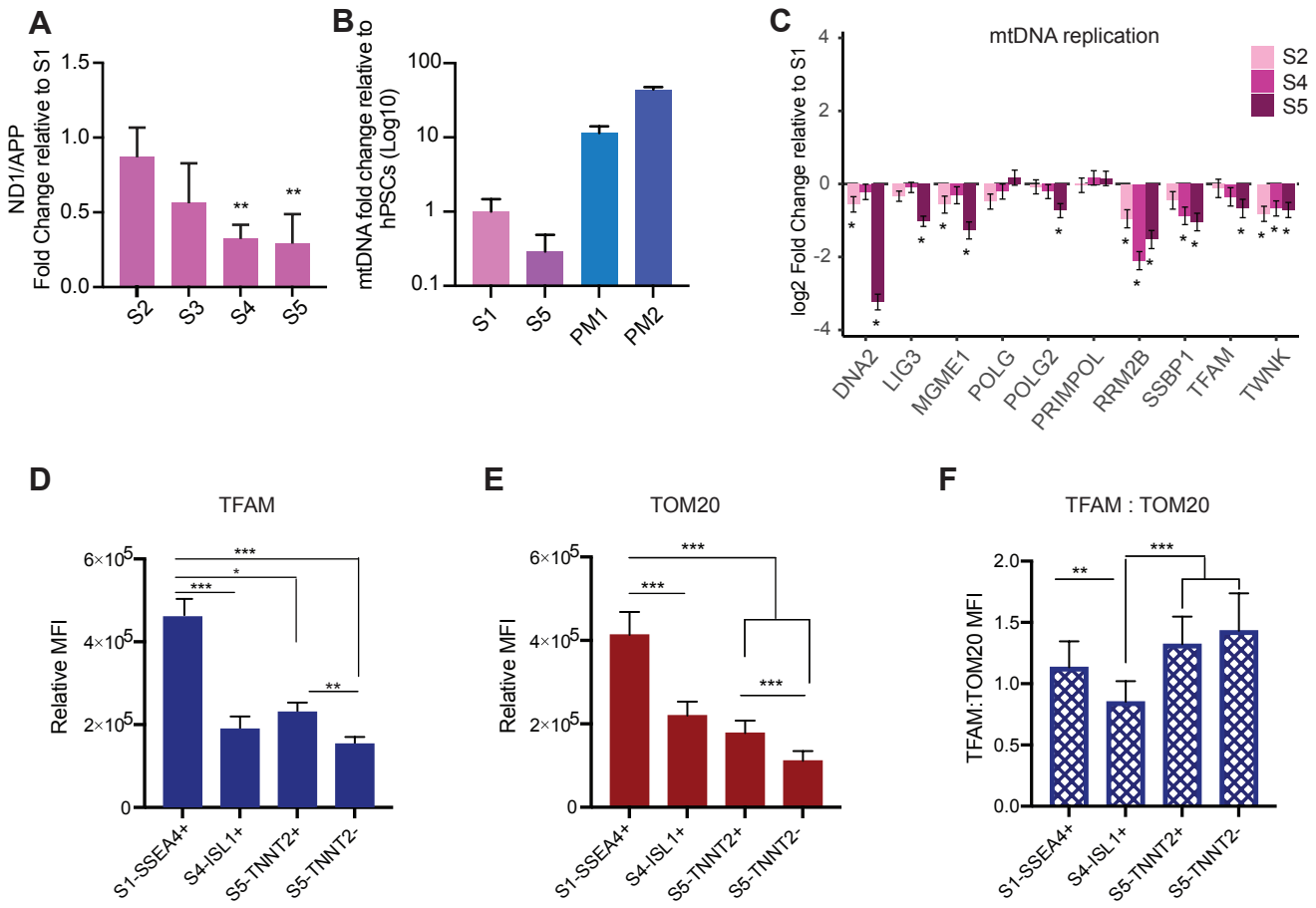

Figure 2) Changes in mitochondrial mass and mtDNA during cardiomyocyte differentiation. **A)** MtDNA copy number fell progressively during cardiomyocytes differentiation. Each bar represents the mean of the mtDNA fold change, pooled data from both hESCs and hiPSCs, at each stage relative to undifferentiated cells at S1 and error bars represent mean values ± 95% c.i., n=11. Statistical significance was assessed using one-way ANOVA followed by Dunnett's post-hoc multiple comparisons. **B)** mtDNA levels were significantly lower in both S1 and S5 cells compared to human heart tissue. The bar chart demonstrates the average mtDNA level in collected cells from all 5 hiPSC lines at S1 (n=9) and S5 (n=8) in comparison with mtDNA level of cells isolated from post-mortem heart tissues (PM1: 59y, female, died of lung cancer, and PM2: 65y, male, died of colon cancer). **C)** Changes in transcriptional level of a battery of genes involved in mtDNA replication and homeostasis at different stages of differentiation relative to undifferentiated stage (S1) in H1 (n=3). **D)** We measured TFAM levels using flow cytometry and detected a significant loss of TFAM at stage S4 and S5 compared with the level at S1. Also, there was a significant difference in TFAM level between TNNT2+ and TNNT2- cells. **E)** We measured TOM20 using flow cytometry and a similar significant decrease at S4 and further reduction was recorded at S5. TNNT2+ demonstrated significantly higher level of TOM20 relative to TNNT2- cells. **F)** The ratio of TFAM:TOM20 increased significantly from stage S4 to stage S5 of cardiac differentiation. Since TFAM binds mtDNA in stoichiometric amounts, this suggests that mtDNA levels have increased per unit mitochondrial volume. In bar charts D-E; each bar represents the mean of the relative median fluorescent intensity (MFI)±s.d., n=18 (SSEA4+ and ISL1+), 20 (TNNT2+/-), and * $P < 0.05$, ** $P < 0.01$ and *** $P < 0.001$.

bioRxiv preprint doi: https://doi.org/10.1101/2021.07.07.451436; this version posted July 7, 2021. The copyright holder for this preprint (which was not certified by peer review) is the author/funder. All rights reserved. No reuse allowed without permission.

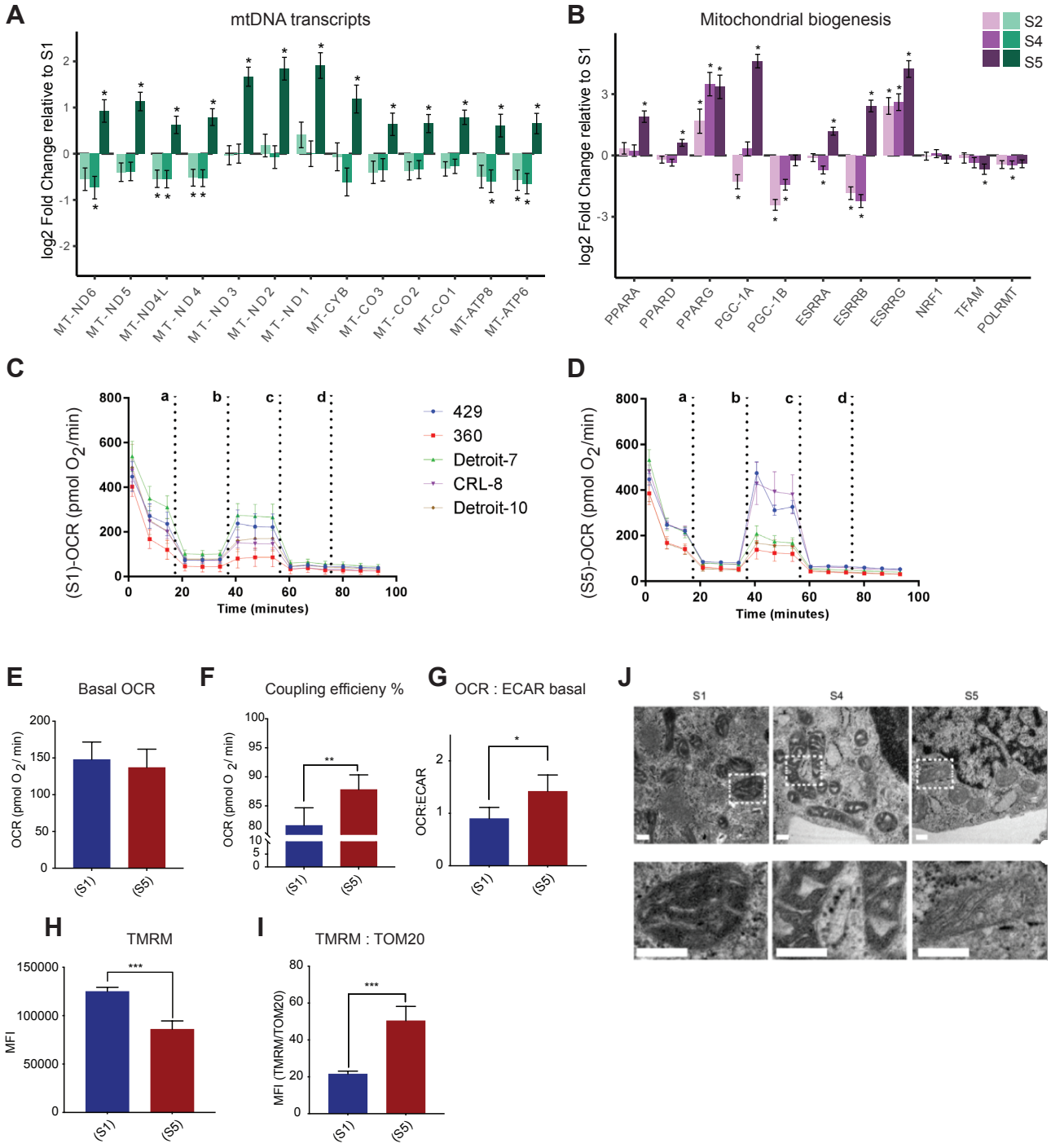

Figure 3) Mitochondria respiration in hPSCs and differentiated mesodermal derivatives. **A)** The mtDNA transcripts collected via RNA-seq at different stages of cardiomyocyte differentiation suggest a significant increase in the number of mitochondrial transcripts in S5 relative to S1, S2 and S4. **B)** A battery of genes associated with metabolic remodeling selected based on previous studies (Scarpulla et al., 2012; Zheng et al., 2016) to evaluate their gene expression changes at different stages of cardiomyocyte differentiation relative to undifferentiated stage S1. Barplots depict the estimated log 2 fold change±s.e.m, n=3. **C and D)** Graphs present the result of oxygen consumption rate (OCR) in hPSCs and differentiated cells at S5. Cells were exposed sequentially to oligomycin (a), CCCP (b), rotenone (c) and antimycin A (d). **E)** To better visualize the result of Seahorse we presented data as bar charts. Basal OCR level didn't change in differentiated cells relative to undifferentiated hPSCs, which suggest higher level of oxygen consumption by differentiated cells since we have shown these cells have almost 50% less mitochondria compare to hPSCs. **F)** Coupling efficiency significantly increased in differentiated cells, which shows the higher potential for ATP generation in differentiated cells relative to undifferentiated hPSCs. **G)** The basal OCR/ECAR showed an increase

bioRxiv preprint doi: https://doi.org/10.1101/2021.07.07.451436; this version posted July 7, 2021. The copyright holder for this preprint (which was not certified by peer review) is the author/funder. All rights reserved. No reuse allowed without permission.

in differentiated cells, which shows these cells are more relay on OXPHOS compare to undifferentiated hPSCs. **H)** We found a high concentration of TMRM in hPSCs relative to S5 cells, however after correction for mitochondrial content in differentiated cells we found (I) a significant increase of TMRM-MFI level in S5 cells relative to undifferentiated hPSCs. **I)** The ratio of TMRM and TOM20 suggested higher level of MMP per unit of mitochondrial mass of differentiated cells compared with undifferentiated hPSCs. Each bar shows mean±s.d., n=3 or 4 independent experiments, and t-test was chosen to assess the statistical significance of the difference between undifferentiated hPSCs and S5. In all bar charts; * $P < 0.05$, ** $P < 0.01$ and *** $P < 0.001$. **J)** Representative TEM pictures of mitochondria during cardiomyocyte differentiation of a hiPSC line (Detroit) at S1, S4 and S5. Mitochondria appear smaller with wider more immature cristae at stages S1 and S4, while at S5, more mitochondria show an expanded matrix with typical, narrow mature cristae. The bottom panel is the magnification of the indicated areas in the upper panel. Scale bar: 200 nm.